Check for updates

Geophysical Research Letters

RESEARCH LETTER
10.1029/2025GL120479

Special Collection:
Space Weather Events of 2024 May 9-15

The May 2024 Storm: The Cusps and Dayside Magnetopause in Simulated Soft X-Rays

J. Ng[1,2], L.-J. Chen[2], B. Burkholder[2,3], D. Sibeck[2], F. S. Porter[2], K. H. Pham[4], V. G. Merkin[5], H. Connor[2], J. W. Bonnell[6], S. Petrinec[7], Y. Zou[5], B. Alterman[2], and G. Cucho-Padin[2]

[1]Department of Astronomy, University of Maryland, College Park, MD, USA, [2]NASA Goddard Space Flight Center, Greenbelt, MD, USA, [3]University of Maryland, Baltimore, MD, USA, [4]High Altitude Observatory, National Center for Atmospheric Research, Boulder, CO, USA, [5]Applied Physics Laboratory, Johns Hopkins University, Laurel, MD, USA, [6]Space Sciences Laboratory, University of California, Berkeley, Berkeley, CA, USA, [7]Lockheed Martin Advanced Technology Center, Palo Alto, CA, USA

Abstract The coronal mass ejection (CME) arriving at Earth on 10 May 2024 caused the most intense geomagnetic storm in the last two decades, resulting in highly unusual cusp and magnetopause dynamics. We simulate soft X-Ray emission due to solar wind charge exchange with exospheric neutrals to image the global dayside dynamics, focusing on the impact of a dense CME current sheet during the storm main phase. The magnetopause moves inward to ∼4 R_E, and the cusps manifest as nearly parallel emission ridges in X-Ray. As the interplanetary magnetic field reverses, the cusp ridges move apart to higher latitudes for ∼10 minutes after the reversal, addressing the open question of how the cusps evolve during and after northward turning of the IMF. Our work highlights soft X-ray imaging enabling simultaneous observations of extreme solar-wind impacts across multiple magnetospheric regions.

Plain Language Summary X-Rays are produced when heavy ions in the solar wind and neutral hydrogen in the vicinity of the Earth interact. When captured by imagers, these X-Rays provide a view of the global magnetospheric structure. On 10 May 2024, a coronal mass ejection (CME) arriving at Earth caused the most intense geomagnetic storm in the last two decades, pushing the boundary between Earth's dipole and the interplanetary magnetic field toward the Earth to ∼4 R_E radial distances. We use simulations to reconstruct how this would have appeared using X-Ray diagnostics, and find that (a) the cusps appear as two parallel emission ridges extending all the way to the magnetopause, and (b) the emission ridges move apart from each other continuously to higher latitudes after the interplanetary magnetic field turns northward. The new results can be tested by missions with X-Ray imaging such as SMILE.

Key Points:

- Reconstructed X-Ray imaging show the cusps as two parallel emission ridges before and during the impact of a dense CME current sheet
- The poleward evolution of the cusp is tracked as B_z turns from southward to northward
- Intense northern over southern cusp asymmetry is seen in X-Ray and driven by the sunward dipole tilt and southward solar wind flow

Supporting Information:

Supporting Information may be found in the online version of this article.

Correspondence to:

L.-J. Chen,
li-jen.chen@nasa.gov

Citation:

Ng, J., Chen, L.-J., Burkholder, B., Sibeck, D., Porter, F. S., Pham, K. H., et al. (2026). The May 2024 storm: The cusps and dayside magnetopause in simulated soft X-rays. *Geophysical Research Letters*, *53*, e2025GL120479. https://doi.org/10.1029/2025GL120479

Received 4 NOV 2025
Accepted 21 AUG 2026

Author Contributions:

Conceptualization: L.-J. Chen, D. Sibeck
Formal analysis: Y. Zou
Funding acquisition: L.-J. Chen
Investigation: J. Ng, L.-J. Chen, B. Burkholder, K. H. Pham, S. Petrinec, Y. Zou

© 2026 The Author(s). Geophysical Research Letters published by Wiley Periodicals LLC on behalf of American Geophysical Union. This article has been contributed to by U.S. Government employees and their work is in the public domain in the USA.
This is an open access article under the terms of the Creative Commons Attribution-NonCommercial License, which permits use, distribution and reproduction in any medium, provided the original work is properly cited and is not used for commercial purposes.

1. Introduction

The May 2024 storm, also known as the Mother's Day storm or the Gannon storm, is the most intense storm in the last two decades. During the storm, the negative peak of Sym-H reached −518 nT (Tulasi Ram et al., 2024), compared to −585 nT of the Hydro-Quebec storm that caused a major power outage across Quebec in 1989 (Boteler et al., 1989). The interplanetary shock arrived at ∼17 UT on 10 May 2024, marking the initial phase of the storm. The strongest current sheet in the CME solar wind is embedded in a high density region (peaking above 100 cm^{-3}) corresponding to the reversal of the interplanetary magnetic field (IMF) with dominant B_y reversing from approximately −60 to 70 nT (Figure 1) during the main phase of the storm. The impact of the IMF reversal and density pulse causes extreme variations (4,300 nT) in geomagnetic fields (Ohtani et al., 2025). The IMF reversal at ∼22:30 UT on May 10 (Figure 1) spans more than 100 R_E transverse to the Sun-Earth line, since both Wind and ACE observe similar IMF profiles at Lagrange point 1. This study focuses on the soft X-Ray perspective of the cusps and dayside magnetopause dynamics around the impact time of this large-scale dense CME current sheet. Soft X-Ray reconstruction for other intervals of the May 2024 storm has been performed to address the magnetopause position variations under changing IMF (Gong et al., 2025), whereas our work highlights the new global features of the cusps.

The capability of soft X-ray imaging to capture the global magnetosphere has been robustly demonstrated. Capitalizing on this technique, several missions have been developed or proposed, including the recent Lunar Environment heliospheric X-ray Imager (LEXI) (B. Walsh et al., 2024), the upcoming Solar wind Magnetosphere

Methodology: D. Sibeck, F. S. Porter, H. Connor, S. Petrinec
Project administration: L.-J. Chen
Resources: Y. Zou
Software: J. Ng, B. Burkholder, K. H. Pham, V. G. Merkin
Validation: S. Petrinec, B. Alterman
Visualization: J. Ng
Writing – original draft: J. Ng, L.-J. Chen
Writing – review & editing: L.-J. Chen, B. Burkholder, D. Sibeck, F. S. Porter, K. H. Pham, V. G. Merkin, H. Connor, J. W. Bonnell, S. Petrinec, Y. Zou, B. Alterman, G. Cucho-Padin

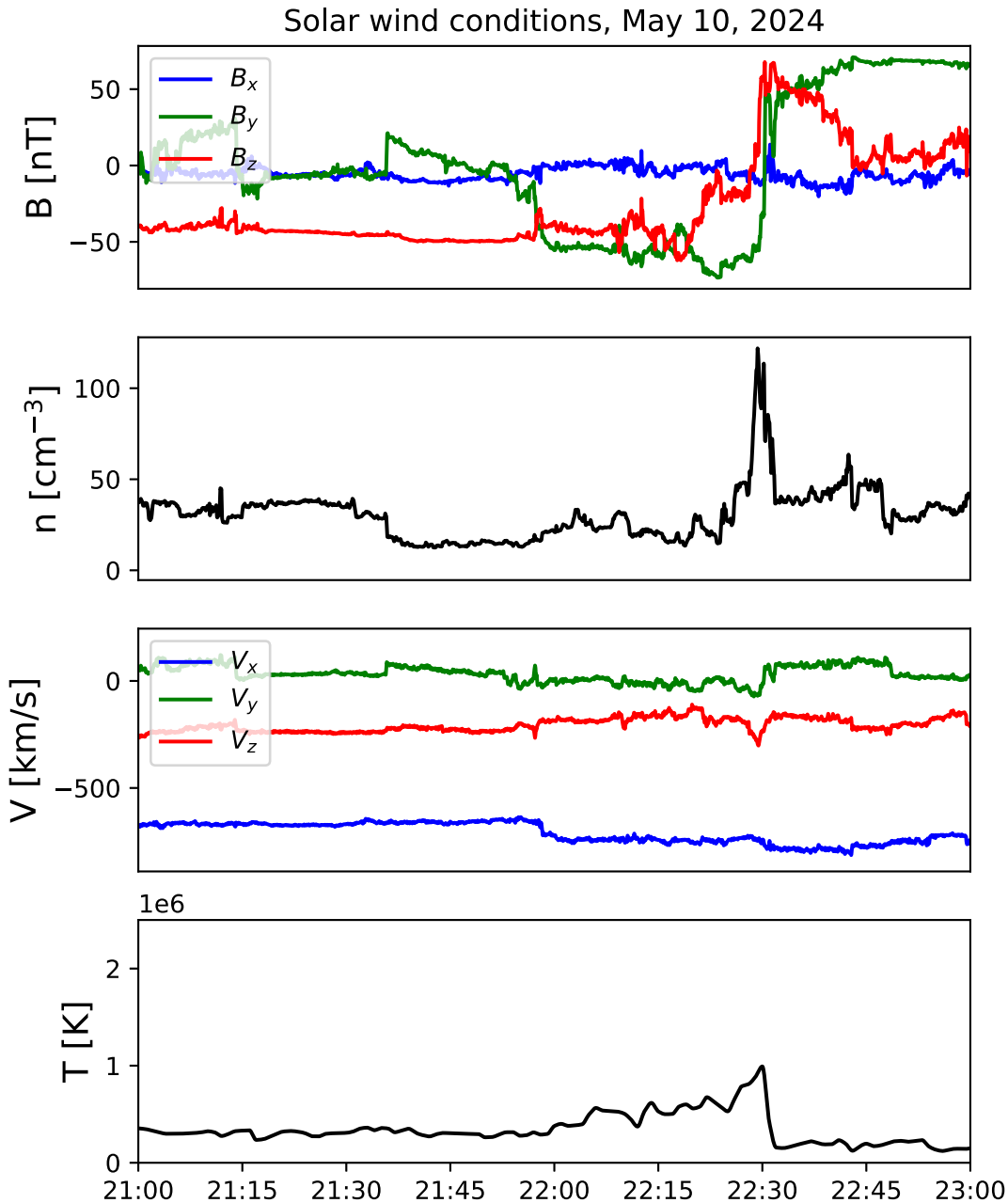


Figure 1. Upstream magnetic field (B), density (n), Velocity (V) and temperature (T) used as the simulation input. The data were measured by MMS1 (B, n, V) and Wind (T), and all data have been time-shifted to the bow shock nose. The reversal of the magnetic field B_y and B_z is associated with a density pulse reaching 120 cm^{-3} and a temperature drop immediately after the density pulse.

Ionosphere Link Explorer (SMILE) (C. Wang et al., 2025), and the Solar-Terrestrial Observer for the Response of the Magnetosphere (STORM) concept (Sibeck et al., 2023). Previous efforts (Kuntz et al., 2015; T. R. Sun et al., 2015; B. M. Walsh, Collier, et al., 2016; T. R. Sun et al., 2019; T. Sun et al., 2021; Connor et al., 2021; Matsumoto & Miyoshi, 2022; Ng et al., 2023; Grandin et al., 2024) have successfully reconstructed expected X-ray images from simulation data, demonstrating the feasibility of observing magnetopause motion, flux transfer events, magnetosheath mirror-mode structures, and the impact of foreshock turbulence. Notably, Sibeck et al. (2018) reviewed foundational work for observing the dayside magnetosphere with wide-field soft X-ray imagers. Building upon this, Sun et al. (2019) used global MHD simulations to show how magnetopause and cusp structures systematically respond to changing solar wind flux and IMF orientations. To extract boundaries

19448007, 2026, 20, Downloaded from https://agupubs.onlinelibrary.wiley.com/doi/10.1029/2025GL120479, Wiley Online Library on [02/11/2026]. See the Terms and Conditions (https://onlinelibrary.wiley.com/terms-and-conditions) on Wiley Online Library for rules of use; OA articles are governed by the applicable Creative Commons License

19448007, 2026, 20, Downloaded from https://agupubs.onlinelibrary.wiley.com/doi/10.1029/2025GL120479, Wiley Online Library on [02/11/2026]. See the Terms and Conditions (https://onlinelibrary.wiley.com/terms-and-conditions) on Wiley Online Library for rules of use; OA articles are governed by the applicable Creative Commons License

from these observations, Sun et al. (2021) developed tangent-fitting techniques capable of reconstructing the large-scale morphology of the cusps. Connor et al. (2021) demonstrated that the X-ray imaging technique captures rapid, global magnetopause dynamics, providing a critical means of remotely monitoring magnetospheric responses to solar wind transients. In this work, we present a novel case study examining the evolution of a large-scale cusp-magnetopause structure driven by a strong, long-duration southward IMF and a subsequent reversal.

Following the modeling process described in detail in Ng et al. (2023), we reconstruct X-ray emission around the impact time of the dense CME current sheet using a soft X-ray model and output from a global geospace simulation driven by spacecraft measurements. Our simulated soft X-ray imaging provides the first global view of the cusps and dayside magnetopause driven by a dense CME current sheet. In Section 2, we discuss the MHD simulations and the X-ray emission model used to calculate the X-ray intensities. In Section 3, we discuss the images produced and the observable physical phenomena, followed by a discussion of future possibilities and a summary in Section 4.

2. Soft X-Ray Model and Global Geospace Simulation

Below, we describe a previously established soft X-ray production model (Connor et al., 2021; Cravens et al., 2001; Kuntz et al., 2015) and data from global geospace simulations of the CME event to reconstruct soft X-ray emission intensity driven by the interaction between solar wind heavy ions and the H in the geocorona.

2.1. Soft X-Ray Model

The X-ray intensity calculation is (Connor et al., 2021; Cravens et al., 2001; Kuntz et al., 2015; Ng et al., 2023):

$$R_{\text{xray}} = \int \frac{\alpha}{4\pi} N_p N_N v_{\text{eff}}\, ds \left[\text{eV cm}^{-2}\ \text{s}^{-1}\ \text{sr}^{-1}\right], \tag{1}$$

where $v_{\text{eff}} = \sqrt{v_b^2 + v_t^2}$ is the effective velocity. v_b is the bulk ion velocity while v_t is the thermal velocity and N_p is the ion density. Due to the nature of the simulation, these are MHD plasma quantities. The integral is line-of-sight and is taken along different angles in the field-of-view of the imager.

The parameter α is a scale factor that determines the soft X-ray production and includes the cross-sections, relative compositions, and transitions for heavy ion states that can give rise to soft X-rays, with $\alpha = 6 \times 10^{-16}$ eV cm^2 for X-rays in the 100 eV to 1 keV range (Connor et al., 2021; Cravens et al., 2001). N_N is the neutral density and we use a profile

$$N_N = 25\left(\frac{10\,R_E}{R}\right)^3 \left[\text{cm}^{-3}\right], \tag{2}$$

where R is the distance from the center of the Earth and R_E is the Earth radius. The value of 25 cm^{-3} is adopted by the SMILE Modeling Working Group for simulating X-ray images and developing image analysis techniques (Connor et al., 2025). Recent studies on geocoronal and soft X-ray observations (Connor & Carter, 2019; Jung et al., 2024, 2025; Zoennchen et al., 2021) showed that the subsolar hydrogen density at 10 R_E is comparable to or higher than 25 cm^{-3}. Thus, 25 cm^{-3} is a good conservative value.

2.2. Global Geospace Simulation Driven by Observations

The global geospace simulations are performed using the Multiscale Atmosphere-Geospace Environment (MAGE) model (Lin et al., 2021; Pham et al., 2022). The MAGE results presented here are from the same run used by Ohtani et al. (2025), and the simulation includes the global MHD model GAMERA (Sorathia et al., 2020; Zhang et al., 2019), the thermosphere-ionosphere coupling model TIE-GCM (Richmond et al., 1992), the ionospheric potential solver REMIX (Merkin & Lyon, 2010), and the inner magnetosphere model RCM (Toffoletto et al., 2003). The configuration of the model is similar to that used by Sorathia et al. (2023) with the inner boundary at 1.5 R_E. The GAMERA warped spherical grid is aligned with the Solar Magnetic (SM) X-direction

19448007, 2026, 20, Downloaded from https://agupubs.onlinelibrary.wiley.com/doi/10.1029/2025GL120479, Wiley Online Library on [02/11/2026]. See the Terms and Conditions (https://onlinelibrary.wiley.com/terms-and-conditions) on Wiley Online Library for rules of use; OA articles are governed by the applicable Creative Commons License

and uses 96 × 96 × 128 cells in the radial, azimuthal, and polar directions, respectively, for simulating this event. The results presented in this work have been interpolated to a uniform Cartesian grid with 0.2 R_E resolution.

For the solar wind and IMF conditions, we use a combined upstream MMS (e.g., Burch et al. (2016); Chen et al. (2024)), ARTEMIS (THEMIS-C specifically) (Artemyev et al., 2018) and Wind (Lepping et al., 1995) data set as input (Figure 1) to MAGE. The MMS spacecraft is just outside of the bow shock and the measurements are more representative of the solar wind conditions immediately upstream of the Earth than those from Lagrange Point 1 (L1, approximately 220 R_E from Earth). Past analysis of the MMS solar wind measurements (e.g.,Roberts et al. (2021)) has indicated that the electron density and ion velocity agree well with the OMNI (King & Papitashvili, 2005) proton density and velocity, while the ion density can be lower than the OMNI proton density (L1 measurements propagated to the bow shock nose). We therefore use the electron density and ion velocity data from the MMS Fast Plasma Investigation (FPI) (Pollock et al., 2016), as well as the magnetic field data from the Flux Gate Magnetometer (Russell et al., 2016). The four MMS satellites are in an electron-scale tetrahedron during the interval of interest, and the measurements do not show discernible differences between satellites. Therefore, only data from MMS1 are shown to represent measurements from the MMS mission. During the time interval displayed, MMS and WIND (temperature) data are used. In Supporting Information S1, we show an extended time interval where the use of different spacecraft data is highlighted, and a more detailed discussion on synthesizing the data sources.

We focus on the interval that encompasses the density pulse at approximately 22:30 UT. There are associated reversals of B_z and B_y, with B_z going from −20 nT to 67 nT over 2 min from 22:28 to 22:30 UT, and B_y going from −61 nT to 54 nT during the same interval.

3. Results

In this Section, we present the dayside magnetosphere in soft X-ray with the X-ray intensity in an example 3D volume rendering and using the results of line of sight integration. The X-Ray intensity at each pixel at 22:36 UT is visualized together with a selection of magnetic field lines (Figure 2, top). IMF field lines are drawn in cyan. Red and green field lines connect to the southern and northern cusps respectively while the magenta field lines are closed. The X-ray signal is strongest in the cusps and in the magnetosheath. The sphere placed at (0, 30 R_E, 0) illustrates a possible position of the imaging spacecraft (taken as the STORM mission) and the yellow line illustrates the line-of-sight along which an integral is taken. The 3D volume rendering represents the integrand of Equation 1, calculated using the output of the global simulation. By tracing magnetic field lines in the interpolated cells around the earth, cells are marked as closed if both ends of the field line they originate from terminate at the inner boundary. The signal in the closed field-line region is set to zero assuming that the high-charge state ions cannot enter the dayside closed-field-line region within the time scale of our study (Küntz et al., 2024; Sibeck et al., 2018). Cells with only one end connected to the inner boundary are still included in the calculation as the high charge state ions can access these regions (e.g., B. M. Walsh, Niehof, et al., 2016; Spjeldvik et al., 2005). A line-of-sight integral is then performed from the imager location. We use the angular resolution of the X-Ray imager in the STORM mission concept (Murphy et al., 2024; Sibeck et al., 2023), designed to study the global solar wind-magnetosphere interaction.

The reconstructed X-ray images of the dayside magnetopause and cusps reveal the 3D magnetosphere reconfiguration around the time of the dense CME current sheet arrival. We follow the evolution using spacecraft placed at (0, $y = 30\,R_E$, 0) and (0, 0, $z = 30\,R_E$) as shown in Figure 2. These are planned locations of the STORM mission, which is intended to have a 30 R_E orbit perpendicular to the ecliptic plane. The angular resolution of the presented data is 0.25° × 0.25°, the intended resolution of the STORM X-Ray imager. Here θ_1 and θ_2 define the viewing angles, with θ_1 corresponding to the looking direction toward different X, and θ_2 the north-south (the "$y = 30\,R_E$" row) or dawn-dusk (the "$z = 30\,R_E$" row) directions.

The arrival of the density pulse can be seen from images at 22:31 to 22:34 UT, with multiple local maxima in the intensity at positive θ_1 corresponding to the density peaks modulated by the $1/R^3$ structure of the neutrals. The innermost intensity peak corresponds to the magnetopause position, where the line of sight viewed from $y = 30\,R_E$ is tangent to the subsolar magnetopause surface. There is an approximate fourfold increase of the peak intensity from 22:31 to 22:34 UT along $\theta_2 = 0$ in the magnetosheath. The magnetopause moves toward Earth from 22:20 to 22:34 UT with the closest distance at ∼4 R_E (Figure 3) as the dense current sheet (IMF reversal and

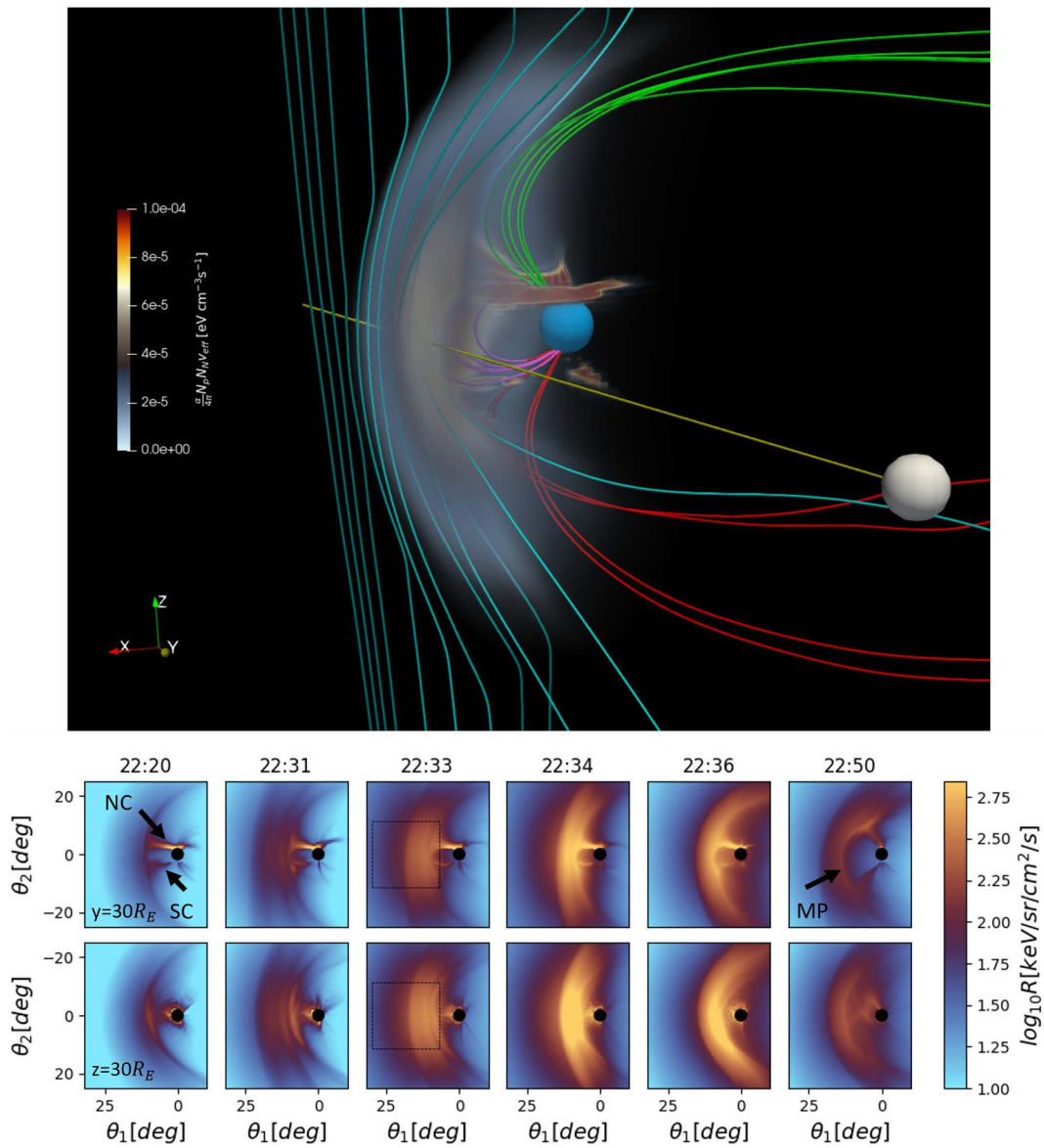


Figure 2. (Top) Volume rendering of the integrand of Equation 1 at 22:36 UT. The white sphere and yellow line show a line-of-sight from a spacecraft positioned at $y = 30\,R_E$ ($x = z = 0$). IMF field lines are drawn in cyan. Red and green field lines connect to the southern and northern cusps respectively. Magenta field lines are closed. (Bottom) Soft X-ray intensity after line of sight integration observed by an imager at [0, 30, 0] R_E (top row) and at [0, 0, 30] R_E (bottom row). The soft X-ray images are constructed with an angular resolution 0.25° × 0.25°. The STORM mission is designed to have an angular resolution 0.17° to 0.25° and a field of view marked by the boxes. Annotations show Northern cusp (NC), Southern cusp (SC) and magnetopause (MP). All vectors are in the SM coordinates.

density pulse) arrives, and the magnetopause expands away from Earth from 22:34 to 22:50 UT as the dense current sheet passes the magnetopause.

The two cusps manifest themselves as two emission ridges in X-Ray with the northern cusp substantially brighter than the southern cusp (Figure 2, top row of thumb-nail panels). This asymmetry is driven by a sunward dipole tilt and a southward component in the solar wind flow (see Figure 1). The two cusp emission ridges are nearly parallel to each other and the sun-earth line until ~22:35 UT, within approximately 2 minutes after the IMF reversal from southward to northward at the magnetopause. Thereafter, the cusp X-Ray emission ridges move poleward, as the magnetopause retreats farther away from Earth. The nearly parallel cusp ridges and the pushed-in magnetopause location indicate that the dayside magnetic flux (closed field lines) is highly eroded as a consequence of the strong

19448007, 2026, 20, Downloaded from https://agupubs.onlinelibrary.wiley.com/doi/10.1029/2025GL120479, Wiley Online Library on [02/11/2026]. See the Terms and Conditions (https://onlinelibrary.wiley.com/terms-and-conditions) on Wiley Online Library for rules of use; OA articles are governed by the applicable Creative Commons License

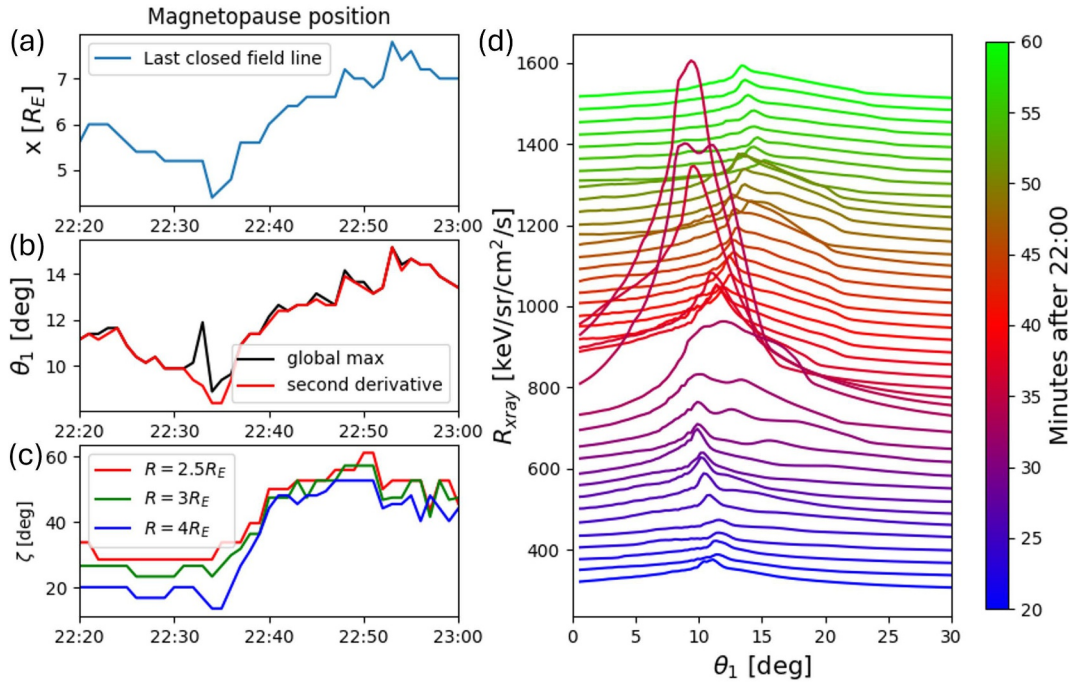


Figure 3. (a) Magnetopause and position determined by magnetic topology and (b) extrema in the X-ray intensity and its second derivative. (c) Angular position of cusp at fixed distance from earth. (d) X-ray intensity as seen from $y = 30\,R_E$ along $\theta_2 = 0$ showing the motion of the magnetopause.

long-duration southward IMF. The strongly eroded magnetopause and parallel shape of the cusp has been seen in other MHD simulations under extreme conditions with southward IMF (Varela et al., 2022; Ngwira et al., 2014).

Inspection of the 3D shape of the open-closed field line boundary reveals that the lower-latitude of the cusp (boundary between closed and half-open field lines) is almost horizontal (with respect to the solar ecliptic plane) over a wide range of Magnetic Local time (MLT). One manifestation is that the emissivity near the lower boundary of the northern cusp appears like a flat disk (top panel in Figure 2).

The northward turning of the IMF starts magnetic reconnection poleward of the cusps, and consequently the two cusp ridges move poleward and away from each other. The motion and orientation of the cusps can be seen in the panel (c) of Figure 3. Here we have defined ζ as $\arctan(z_c/x_c)$, where z_c, x_c are the coordinates of the open-closed boundary in the plane $y = 0$ at a fixed distance R from the earth. This quantity is calculated for different R, and increases after 22:35 UT, corresponding to the poleward motion of the cusps. The larger discrepancy between the values at different R before the northward turning of the IMF is due to the flatter orientation of the cusp.

We estimate the poleward velocity of the cusp using the evolution of magnetic topology and the peak intensity of cusp X-ray emission. At $4\,R_E$, the open-closed boundary at $y = 0$ moves at approximately 50 km/s between 22:35 and 22:40 UT. To obtain an estimate from the X-ray images taken at $y = 30\,R_E$, we map points with $y = 0$, $x^2 + z^2 = 4\,R_E$ to viewing angles θ_1, θ_2, then calculate the motion of the point with maximum intensity. This can then be converted into a measurement of poleward velocity, from which we obtain a maximum of approximately 40 km/s during the turning of the IMF, which is of the same order as the measurement using the magnetic topology, and approximately consistent with Cluster multi-spacecraft in-situ observations of cusp velocity ($\sim$30 km/s at $\sim 5\,R_E$) as the IMF turns northward (Pitout et al., 2006). Here we use the maximum intensity to maintain consistency while calculating the position of the cusp. We note that using the point of maximum emission will track the location at the center of the cusp (T. Sun et al., 2021), and can only be used for poleward velocity estimates for certain imager positions such as the one used in this paper, which is an ideal case and a planned viewing configuration of the STORM mission concept (Sibeck et al., 2018). For the more general case, the cusp boundaries can be tracked by finding sudden variations of the X-ray intensity, and the projection in the x-z plane estimated by assuming a specific cross-sectional shape such as an ellipse (X. Wang et al., 2026).

19448007, 2026, 20, Downloaded from https://agupubs.onlinelibrary.wiley.com/doi/10.1029/2025GL120479, Wiley Online Library on [02/11/2026]. See the Terms and Conditions (https://onlinelibrary.wiley.com/terms-and-conditions) on Wiley Online Library for rules of use; OA articles are governed by the applicable Creative Commons License

19448007, 2026, 20, Downloaded from https://agupubs.onlinelibrary.wiley.com/doi/10.1029/2025GL120479, Wiley Online Library on [02/11/2026]. See the Terms and Conditions (https://onlinelibrary.wiley.com/terms-and-conditions) on Wiley Online Library for rules of use; OA articles are governed by the applicable Creative Commons License

X-Ray imaging provides a global view of the magnetic flux erosion and re-generation processes, and a possibility to quantify the variation of the flux content as well as the time scale. For example, the addition of flux to the dayside can be seen through both the displacement of the magnetopause in the positive θ_1 direction as well as the cusp moving poleward. The area corresponding to the closed-field-line-region (bounded by the two cusps and the magnetopause) of the magnetosphere in the reconstructed images is approximately four times larger at 22:50 UT compared to that at 22:34 UT.

As mentioned earlier, the magnetopause position can be identified by finding the peak intensity along θ_1, or a peak in its second derivative (Collier & Connor, 2018; Connor et al., 2021). The motion of the magnetopause is illustrated in Figure 3. Panel (a) shows the location of the last closed field line along x at $y = 0, z = 0$ in the simulation, and there is abrupt inward displacement of the magnetopause to within 4–5 R_E radial distances at around 22:34 UT, followed by relaxation. This unusually short distance of the magnetopause standing off the CME wind is consistent with observations by THEMIS [constrained to be <6 R_E (Fu et al., 2025)] and Arase ($\sim$5–6 R_E (Miyoshi et al., 2025)) spacecraft. Panel (b) shows the magnetopause position inferred from the X-ray intensity using either the maximum intensity or the minimum of $d^2R_{\mathrm{xray}}/d\theta_1^2$. Both methods produce general agreement with the result from magnetic topology, despite a discrepancy in position from 22:32 to 22:35 UT, with the maximum intensity method showing a more sunward magnetopause position. The cause is illustrated in the panel (d), which shows the variation in intensity along θ_1 at $\theta_2 = 0$, in which the colors represent time. The arrival of the CME current sheet can be seen in the increase of the X-ray intensity sunward of the magnetopause (larger θ_1), with the maximum intensity observed due to the dense current sheet rather than the magnetopause boundary at certain times. More complex methods exist that extract the magnetopause location in GSE coordinates from soft X-ray emission peak angles and determine the shape of magnetopause (e.g., Collier & Connor, 2018; Kim et al., 2023; Cucho-Padin et al., 2024; Gong et al., 2025).

What would the STORM soft X-Ray imager observe under extreme solar wind conditions such as the May 2024 storm? In Figure 2 we show the expected results using the field of view of the proposed STORM imager, which is 23° × 23° field of view pointed 18.5° sunward of nadir, and is illustrated by the dashed box in Figure 2. STORM will be able to track the magnetopause position over time, as the density pulse pushes the subsolar magnetopause closer and closer to Earth up to $\sim$4 R_E radial distance. At 22:34 UT, when the magnetopause position reaches $X \sim$ 4–5 R_E, the subsolar magnetopause is still visible, although it is close to the Earthward edge of the planned field of view of the STORM imager.

The question of whether this X-ray signal can be measured is important. The results thus far are instantaneous, whereas an actual instrument would have finite time integration and be affected by backgrounds. During the arrival of the CME current sheet, the peak intensity in the magnetosheath is over 800 keV cm^{-2} s^{-1} sr^{-1}, compared to the diffuse soft X-ray background of 10–30 keV cm^{-2} s^{-1} sr^{-1} (Sibeck et al., 2018). Based on previous work on reconstructions (B. M. Walsh, Collier, et al., 2016), this unusually high signal from the magnetosheath, because of the high density, would enable high cadence (sub 1 min) images to be captured. The location of the cusp and magnetopause introduce the possibility of contamination due to ultraviolet emissions. This includes He$^+$ 30.4 nm emission from the plasmasphere and H Lyamn-α emission from the exosphere. The expected intensities are up to 10 Rayleigh from the plasmasphere (He et al., 2013), and around 3 to 5 kRayleigh from the exosphere (Cucho-Padin & Waldrop, 2018). LEXI and SMILE use blocking filters to attenuate the UV contamination of similar intensities (B. Walsh et al., 2024; Sembay et al., 2025), and residual emission can be accounted for by modeling (B. M. Walsh et al., 2021).

4. Summary and Discussion

Our simulated soft X-Ray images reveal the global dynamics of the cusps and dayside magnetopause during the May 2024 storm, particularly in response to prolonged strong southward IMF and an unusually dense CME current sheet. Using the MAGE global simulations of the 10 May 2024 CME event, we reconstruct the X-Ray images expected to be measured by spacecraft located at (0, 30 R_E, 0) and (0, 0, 30 R_E). The combined X-Ray and global simulation results show that (a) the variation of the angle of maximum emissivity corresponding to the position of the magnetopause shows that it moves earthward during the arrival of the CME sheet, consistent with spacecraft observations and field-line-tracing simulation results, (b) the cusps in X-ray emissions move poleward from nearly parallel to each other with a time delay a few minutes after the IMF B_z turns from southward to northward at the subsolar magnetopause, and the migration to higher and higher latitudes occurs over $\sim$10

19448007, 2026, 20, Downloaded from https://agupubs.onlinelibrary.wiley.com/doi/10.1029/2025GL120479, Wiley Online Library on [02/11/2026]. See the Terms and Conditions (https://onlinelibrary.wiley.com/terms-and-conditions) on Wiley Online Library for rules of use; OA articles are governed by the applicable Creative Commons License

minutes. The X-ray images are also used to estimate the velocity of the poleward motion. (c) The northern cusp is substantially brighter in X-Ray than the southern cusp. This pronounced asymmetry is due to the combination of a sunward dipole tilt of 18.3° and a southward component in the solar wind flow ($V_z \sim 250$ km/s—see Figure 1). The sunward tilt geometrically exposes the northern cusp to the upstream flow, while the southward velocity of the solar wind rams plasma more directly into the northern than the southern hemisphere. Consequently, a significantly higher flux of solar wind ions is funneled into the northern cusp, driving a localized increase in solar-wind-charge-exchange collisions and resulting in the enhanced X-ray brightness.

The global X-ray view of the magnetopause and cusps complements those from the ionospheric measurements. Based on ionospheric radar measurements from the SuperDARN network (Greenwald et al., 1995), the open-close magnetic field boundary (the low-latitude boundary of the cusp) at ~22:20 UT is at MLAT ~56°, and at 22:50 UT, it is further poleward between 62° and 66°. Using a composite model of the cusp location and extent at ionospheric altitudes (constructed from empirical relations of dependences on solar wind conditions and the dipole tilt angle in the literature) (Petrinec et al., 2023) for a southward IMF $B_z = -50$ nT (such as the B_z at 22:20 UT, Figure 1) and a dipole tilt of 18.3°, the equatorward edge of the northern cusp is obtained to be 58–59°, consistent with the radar observation. When the IMF is northward with $B_z \sim 50$ nT (just after the large IMF B_y rotation, Figure 1) the equatorward edge of the northern cusp is at ~85° based on the model. The X-Ray picture shows the large-scale cusp structure in a radial distance range ~1.5 R_E to ~5 R_E, and its evolution from approximately perpendicular to forming an acute angle with respect to the dipole axis (along positive z in the SM coordinate used in this paper), information not available from the ionospheric measurements or the empirical cusp model.

Soft X-ray imaging enables simultaneous observations of solar-wind impacts across multiple magnetospheric regions. As such, it complements in situ measurements of the magnetospheric plasma by providing the global context, such as the locations and structures of the magnetopause, cusps, the bow shock, and magnetosheath. The global X-ray images from future missions will provide large-scale information that is challenging, if not impossible, for even multi-point local measurements to deliver.

Conflict of Interest

The authors declare no conflicts of interest relevant to this study.

Availability Statement

The data sets analyzed in this study are publicly accessible at Ng et al. (2025).

Acknowledgments
The work of JN, LJC, and BB was supported by the NASA MMS mission, and the work of KHP and VGM by the NASA DRIVE Science Center for Geospace Storms (CGS) under NASA award 80NSSC22M0163. JN was also supported by NASA Grant 80NSSC24K0094. The MAGE model is developed by CGS. We acknowledge high-performance computing support from NASA High-End-Computing and the Derecho system (https://doi.org/10.5065/qx9a-pg09) provided by the NSF National Center for Atmospheric Research (NCAR), sponsored by the National Science Foundation.

References

Artemyev, A. V., Angelopoulos, V., & McTiernan, J. M. (2018). Near-earth solar wind: Plasma characteristics from Artemis measurements. *Journal of Geophysical Research: Space Physics*, *123*(12), 9955–9962. https://doi.org/10.1029/2018JA025904

Boteler, D., Shier, R., Watanabe, T., & Horita, R. (1989). Effects of geomagnetically induced currents in the BC hydro 500 kV system. *IEEE Transactions on Power Delivery*, *4*(1), 818–823. https://doi.org/10.1109/61.19275

Burch, J., Torbert, R., Phan, T., Chen, L.-J., Moore, T., Ergun, R., et al. (2016). Electron-scale measurements of magnetic reconnection in space. *Science*, *352*(6290), aaf2939. https://doi.org/10.1126/science.aaf2939

Chen, L.-J., Gershman, D., Burkholder, B., Chen, Y., Sarantos, M., Jian, L., et al. (2024). Earth's Alfvén wings driven by the April 2023 coronal mass ejection. *Geophysical Research Letters*, *51*(14), e2024GL108894. https://doi.org/10.1029/2024GL108894

Collier, M. R., & Connor, H. K. (2018). Magnetopause surface reconstruction from tangent vector observations. *Journal of Geophysical Research: Space Physics*, *123*(12), 10189–10199. https://doi.org/10.1029/2018JA025763

Connor, H. K., & Carter, J. A. (2019). Exospheric neutral hydrogen density at the nominal 10 re subsolar point deduced from XMM-newton x-ray observations. *Journal of Geophysical Research: Space Physics*, *124*(3), 1612–1624. https://doi.org/10.1029/2018ja026187

Connor, H. K., Sibeck, D. G., Collier, M. R., Baliukin, I. I., Branduardi-Raymont, G., Brandt, P. C., et al. (2021). Soft x-ray and ENA imaging of the Earth's dayside magnetosphere. *Journal of Geophysical Research: Space Physics*, *126*(3), e2020JA028816. https://doi.org/10.1029/2020JA028816

Connor, H. K., Sun, T., Samsonov, A., Liang, J., Read, A., Li, D., et al. (2025). Smile modeling working group: Modeling and analysis of x-ray and ultraviolet images of solar wind–earth interactions. *Space Science Reviews*, *221*(4), 46. https://doi.org/10.1007/s11214-025-01172-8

Cravens, T. E., Robertson, I. P., & Snowden, S. L. (2001). Temporal variations of geocoronal and heliospheric x-ray emission associated with the solar wind interaction with neutrals. *Journal of Geophysical Research*, *106*(A11), 24883–24892. https://doi.org/10.1029/2000JA000461

Cucho-Padin, G., Connor, H., Jung, J., Walsh, B., & G. Sibeck, D. (2024). Finding the magnetopause location using soft x-ray observations and a statistical inverse method. *Earth and Planetary Physics*, *8*(1), 184–203. https://doi.org/10.26464/epp2023070

Cucho-Padin, G., & Waldrop, L. (2018). Tomographic estimation of exospheric hydrogen density distributions. *Journal of Geophysical Research: Space Physics*, *123*(6), 5119–5139. https://doi.org/10.1029/2018JA025323

Fu, W. D., Fu, H. S., Zhang, W. Z., Yu, Y., & Cao, J. B. (2025). Compression of earth's magnetopause down to 5 Re during the superstorm on 10 May 2024. *Geophysical Research Letters*, *52*(5), e2024GL114040. https://doi.org/10.1029/2024GL114040

Gong, Y., Sun, T., Tang, B., Guo, Y., Sembay, S., & Wang, C. (2025). Dynamic x-ray imaging of the magnetosheath expected during a super storm. *Frontiers in Astronomy and Space Sciences*, *12*, 1563653. https://doi.org/10.3389/fspas.2025.1563653

Grandin, M., Connor, H. K., Hoilijoki, S., Battarbee, M., Pfau-Kempf, Y., Ganse, U., et al. (2024). Hybrid-Vlasov simulation of soft x-ray emissions at the Earth's dayside magnetospheric boundaries. *Earth and Planetary Physics*, *8*(1), 70–88. https://doi.org/10.26464/epp2023052

Greenwald, R., Baker, K., Dudeney, J., Pinnock, M., Jones, T., Thomas, E., et al. (1995). Darn/superdarn: A global view of the dynamics of high-latitude convection. *Space Science Reviews*, *71*(1), 761–796. https://doi.org/10.1007/bf00751350

He, F., Zhang, X.-X., Chen, B., Fok, M.-C., & Zou, Y.-L. (2013). Moon-based EUV imaging of the Earth's plasmasphere: Model simulations. *Journal of Geophysical Research: Space Physics*, *118*(11), 7085–7103. https://doi.org/10.1002/2013JA018962

Jung, J., Connor, H., Dimmock, A., Sembay, S., Read, A., & Soucek, J. (2024). Mshpy23: A user-friendly, parameterized model of magnetosheath conditions. *Earth and Planetary Physics*, *8*(1), 89–104. https://doi.org/10.26464/epp2023065

Jung, J., Connor, H. K., Carter, J. A., Koutroumpa, D., & Pagani, C. (2025). Exospheric neutral density at the 10 re subsolar point during solar maximum: Estimates from XMM soft x-ray observations. *Frontiers in Astronomy and Space Sciences*, *12*, 1568929. https://doi.org/10.3389/fspas.2025.1568929

Kim, H., Connor, H. K., Jung, J., Walsh, B. M., Sibeck, D., Kuntz, K. D., et al. (2023). Estimating the subsolar magnetopause position from soft x-ray images using a low-pass image filter. *Earth and Planetary Physics*, *8*(1).

King, J. H., & Papitashvili, N. E. (2005). Solar wind spatial scales in and comparisons of hourly wind and ace plasma and magnetic field data. *Journal of Geophysical Research*, *110*(A2). https://doi.org/10.1029/2004JA010649

Kuntz, K. D., Collado-Vega, Y. M., Collier, M. R., Connor, H. K., Cravens, T. E., Koutroumpa, D., et al. (2015). The solar wind charge-exchange production factor for hydrogen. *The Astrophysical Journal*, *808*(2), 143. https://doi.org/10.1088/0004-637X/808/2/143

Küntz, K. D., Koutroumpa, D., Dunn, W. R., Foster, A., Porter, F. S., Sibeck, D. G., et al. (2024). The magnetosheath at high spectral resolution. *Earth and Planetary Physics*, *8*(1), 234–246. https://doi.org/10.26464/epp2023060

Lepping, R., Acũna, M., Burlaga, L., Farrell, W., Slavin, J., Schatten, K., et al. (1995). The wind magnetic field investigation. *Space Science Reviews*, *71*(1), 207–229. https://doi.org/10.1007/bf00751330

Lin, D., Sorathia, K., Wang, W., Merkin, V., Bao, S., Pham, K., et al. (2021). The role of diffuse electron precipitation in the formation of subauroral polarization streams. *Journal of Geophysical Research: Space Physics*, *126*(12), e2021JA029792. https://doi.org/10.1029/2021JA029792

Matsumoto, Y., & Miyoshi, Y. (2022). Soft x-ray imaging of magnetopause reconnection outflows under low plasma-β solar wind conditions. *Geophysical Research Letters*, *49*(19), e2022GL101037. https://doi.org/10.1029/2022GL101037

Merkin, V. G., & Lyon, J. G. (2010). Effects of the low-latitude ionospheric boundary condition on the global magnetosphere. *Journal of Geophysical Research*, *115*(A10). https://doi.org/10.1029/2010JA015461

Miyoshi, Y., Shinohara, I., Takashima, T., Asamura, K., Mitani, T. A. H. N., Kasahara, S., et al. (2025). Arase observations of the radiation belts during the May 2024 geomagnetic storm. In *EGU General Assembly, EGU25-5458*. https://doi.org/10.5194/egusphere-egu25-5458

Murphy, K. R., Shoemaker, M. A., Sibeck, D. G., Schiff, C., Connor, H., Porter, F. S., & Zesta, E. (2024). Target and science visibility of the solar-terrestrial observer for the response of the magnetosphere (storm) global imaging mission concept. *Frontiers in Astronomy and Space Sciences*, *11*, 1394655. https://doi.org/10.3389/fspas.2024.1394655

Ng, J., Burkholder, B., Chen, L.-J., Merkin, V. G., Pham, K. H., Sibeck, D., et al. (2025). Dataset for: "the May 2024 storm: Dayside magnetopause and cusps in simulated soft x-rays" [Dataset]. *Zenodo*. https://doi.org/10.5281/zenodo.17179578

Ng, J., Walsh, B. M., Chen, L.-J., & Omelchenko, Y. (2023). Soft x-ray imaging of earth's dayside magnetosheath and cusps using hybrid simulations. *Geophysical Research Letters*, *50*(10), e2023GL103347. https://doi.org/10.1029/2023GL103347

Ngwira, C. M., Pulkkinen, A., Kuznetsova, M. M., & Glocer, A. (2014). Modeling extreme "Carrington-type" space weather events using three-dimensional global MHD simulations. *Journal of Geophysical Research: Space Physics*, *119*(6), 4456–4474. https://doi.org/10.1002/2013JA019661

Ohtani, S., Zou, Y., Merkin, V. G., Wiltberger, M., Pham, K. H., Raptis, S., et al. (2025). Ground magnetic response to an extraordinary IMF by flip during the May 2024 storm: Travel time from the magnetosheath to dayside high latitudes. *Journal of Geophysical Research: Space Physics*, *130*(5), e2024JA033691. https://doi.org/10.1029/2024JA033691

Petrinec, S. M., Kletzing, C. A., Bounds, S. R., Fuselier, S. A., Trattner, K. J., & Sawyer, R. P. (2023). Trice-2 rocket observations in the low-altitude cusp: Boundaries and comparisons with models. *Journal of Geophysical Research: Space Physics*, *128*(3), e2022JA030952. https://doi.org/10.1029/2022JA030952

Pham, K. H., Zhang, B., Sorathia, K., Dang, T., Wang, W., Merkin, V., et al. (2022). Thermospheric density perturbations produced by traveling atmospheric disturbances during August 2005 storm. *Journal of Geophysical Research: Space Physics*, *127*(2), e2021JA030071. https://doi.org/10.1029/2021JA030071

Pitout, F., Escoubet, C. P., Bogdanova, Y. V., Georgescu, E., Fazakerley, A. N., & Rème, H. (2006). Response of the mid-altitude cusp to rapid rotations of the IMF. *Geophysical Research Letters*, *33*(11). https://doi.org/10.1029/2005GL025460

Pollock, C., Moore, T., Jacques, A., Burch, J., Gliese, U., Saito, Y., et al. (2016). Fast plasma investigation for magnetospheric multiscale. *Space Science Reviews*, *199*(1–4), 331–406. https://doi.org/10.1007/s11214-016-0245-4

Richmond, A. D., Ridley, E. C., & Roble, R. G. (1992). A thermosphere/ionosphere general circulation model with coupled electrodynamics. *Geophysical Research Letters*, *19*(6), 601–604. https://doi.org/10.1029/92GL00401

Roberts, O. W., Nakamura, R., Coffey, V. N., Gershman, D. J., Volwerk, M., Varsani, A., et al. (2021). A study of the solar wind ion and electron measurements from the magnetospheric multiscale mission's fast plasma investigation. *Journal of Geophysical Research: Space Physics*, *126*(10), e2021JA029784. https://doi.org/10.1029/2021JA029784

Russell, C., Anderson, B., Baumjohann, W., Bromund, K., Dearborn, D., Fischer, D., et al. (2016). The magnetospheric multiscale magnetometers. *Space Science Reviews*, *199*(1), 189–256. https://doi.org/10.1007/s11214-014-0057-3

Sembay, S., Cheney, A., Hampson, R., Agnolon, D., Arnold, T., Beardmore, A., et al. (2025). The soft x-ray imager (SXI) on the smile mission. *Space Science Reviews*, *221*(8), 113. https://doi.org/10.1007/s11214-025-01241-y

Sibeck, D. G., Allen, R., Aryan, H., Bodewits, D., Brandt, P., Branduardi-Raymont, G., et al. (2018). Imaging plasma density structures in the soft x-rays generated by solar wind charge exchange with neutrals. *Space Science Reviews*, *214*(4), 1–124. https://doi.org/10.1007/s11214-018-0504-7

Sibeck, D. G., Murphy, K. R., Porter, F. S., Connor, H. K., Walsh, B. M., Kuntz, K. D., et al. (2023). Quantifying the global solar wind-magnetosphere interaction with the solar-terrestrial observer for the response of the magnetosphere (storm) mission concept. *Frontiers in Astronomy and Space Sciences*, *10*, 1138616. https://doi.org/10.3389/fspas.2023.1138616

19448007, 2026, 20, Downloaded from https://agupubs.onlinelibrary.wiley.com/doi/10.1029/2025GL120479, Wiley Online Library on [02/11/2026]. See the Terms and Conditions (https://onlinelibrary.wiley.com/terms-and-conditions) on Wiley Online Library for rules of use; OA articles are governed by the applicable Creative Commons License

Sorathia, K. A., Merkin, V. G., Panov, E. V., Zhang, B., Lyon, J. G., Garretson, J., et al. (2020). Ballooning-interchange instability in the near-earth plasma sheet and auroral beads: Global magnetospheric modeling at the limit of the MHD approximation. *Geophysical Research Letters*, *47*(14), e2020GL088227. https://doi.org/10.1029/2020GL088227

Sorathia, K. A., Michael, A., Merkin, V. G., Ohtani, S., Keesee, A. M., Sciola, A., et al. (2023). Multiscale magnetosphere-ionosphere coupling during stormtime: A case study of the dawnside current wedge. *Journal of Geophysical Research: Space Physics*, *128*(11), e2023JA031594. https://doi.org/10.1029/2023JA031594

Spjeldvik, W., Fritz, T., Chen, J., & Zong, Q.-G. (2005). Energetic ion observations of the earth's magnetic cusps during an extended geomagnetically quiescent period in April 2001 using detectors on S/C ISTP/Polar. *Advances in Space Research*, *36*(10), 1946–1950. https://doi.org/10.1016/j.asr.2004.07.015

Sun, T., Wang, X., & Wang, C. (2021). Tangent directions of the cusp boundary derived from the simulated soft x-ray image. *Journal of Geophysical Research: Space Physics*, *126*(3), e2020JA028314. https://doi.org/10.1029/2020JA028314

Sun, T. R., Wang, C., Sembay, S. F., Lopez, R. E., Escoubet, C. P., Branduardi-Raymont, G., et al. (2019). Soft x-ray imaging of the magnetosheath and cusps under different solar wind conditions: Mhd simulations. *Journal of Geophysical Research: Space Physics*, *124*(4), 2435–2450. https://doi.org/10.1029/2018JA026093

Sun, T. R., Wang, C., Wei, F., & Sembay, S. (2015). X-ray imaging of Kelvin-Helmholtz waves at the magnetopause. *Journal of Geophysical Research: Space Physics*, *120*(1), 266–275. https://doi.org/10.1002/2014JA020497

Toffoletto, F., Sazykin, S., Spiro, R., & Wolf, R. (2003). Inner magnetospheric modeling with the rice convection model. *Space Science Reviews*, *107*(1–2), 175–196. https://doi.org/10.1023/a:1025532008047

Tulasi Ram, S., Veenadhari, B., Dimri, A. P., Bulusu, J., Bagiya, M., Gurubaran, S., et al. (2024). Super-intense geomagnetic storm on 10–11 May 2024: Possible mechanisms and impacts. *Space Weather*, *22*(12), e2024SW004126. https://doi.org/10.1029/2024SW004126

Varela, J., Brun, A. S., Strugarek, A., Réville, V., Zarka, P., & Pantellini, F. (2022). Mhd study of the planetary magnetospheric response during extreme solar wind conditions: Earth and exoplanet magnetospheres applications. *A&A*, *659*, A10. https://doi.org/10.1051/0004-6361/202141181

Walsh, B., Kuntz, K., Busk, S. E., Cameron, T., Chornay, D., Chuchra, A., et al. (2024). The lunar environment heliophysics x-ray imager (LEXI) mission. *Space Science Reviews*, *220*(4), 37. https://doi.org/10.1007/s11214-024-01063-4

Walsh, B. M., Collier, M. R., Atz, E., Billingsley, L., Broll, J. M., Connor, H. K., et al. (2021). The cusp plasma imaging detector (CUPID) CubeSat observatory: Mission overview. *Journal of Geophysical Research: Space Physics*, *126*(4), e2020JA029015. https://doi.org/10.1029/2020JA029015

Walsh, B. M., Collier, M. R., Kuntz, K. D., Porter, F. S., Sibeck, D. G., Snowden, S. L., et al. (2016). Wide field-of-view soft x-ray imaging for solar wind-magnetosphere interactions. *Journal of Geophysical Research: Space Physics*, *121*(4), 3353–3361. https://doi.org/10.1002/2016JA022348

Walsh, B. M., Niehof, J., Collier, M. R., Welling, D. T., Sibeck, D. G., Mozer, F. S., et al. (2016). Density variations in the Earth's magnetospheric cusps. *Journal of Geophysical Research: Space Physics*, *121*(3), 2131–2142. https://doi.org/10.1002/2015JA022095

Wang, C., Branduardi-Raymont, G., Escoubet, C. P., & Forsyth, C. (2025). Solar wind magnetosphere ionosphere link explorer (smile): Science and mission overview. *Space Science Reviews*, *221*(1), 9. https://doi.org/10.1007/s11214-024-01126-6

Wang, X., Sun, T., Escoubet, C. P., Read, A., Guo, Y., Sembay, S., & Wang, C. (2026). Tracing equatorward and poleward boundaries of the magnetospheric cusp from a simulated x-ray image. *Earth and Planetary Physics*, *10*(1), 144–155. https://doi.org/10.26464/epp2026013

Zhang, B., Sorathia, K. A., Lyon, J. G., Merkin, V. G., Garretson, J. S., & Wiltberger, M. (2019). Gamera: A three-dimensional finite-volume MHD solver for non-orthogonal curvilinear geometries. *The Astrophysical Journal Supplement Series*, *244*(1), 20. https://doi.org/10.3847/1538-4365/ab3a4c

Zoennchen, J. H., Connor, H. K., Jung, J., Nass, U., & Fahr, H. J. (2021). Terrestrial exospheric dayside h-density profile at 3–15 r_e from UVIS/HDAC and twins Lyman-α data combined. *Annales Geophysicae Discussions*, *2021*, 1–16.

References From the Supporting Information

Espinoza, J. M., & Borovsky, J. E. (2025). The connection of the ions and electrons in the earth's central plasma sheet to the solar wind. *Frontiers in Astronomy and Space Sciences*, *12*, 1672108. https://doi.org/10.3389/fspas.2025.1672108

19448007, 2026, 20, Downloaded from https://agupubs.onlinelibrary.wiley.com/doi/10.1029/2025GL120479, Wiley Online Library on [02/11/2026]. See the Terms and Conditions (https://onlinelibrary.wiley.com/terms-and-conditions) on Wiley Online Library for rules of use; OA articles are governed by the applicable Creative Commons License